The Astrophysical Journal, 911:86 (11pp), 2021 April 20 https://doi.org/10.3847/1538-4357/abe85a
© 2021. The American Astronomical Society. All rights reserved.

The Evolution of Plasma Composition during a Solar Flare

Andy S. H. To[1], David M. Long[1], Deborah Baker[1], David H. Brooks[2], Lidia van Driel-Gesztelyi[1,3,4], J. Martin Laming[5], and Gherardo Valori[1]

[1] University College London, Mullard Space Science Laboratory, Holmbury St. Mary, Dorking, Surrey, RH5 6NT, UK
[2] College of Science, George Mason University, 4400 University Drive, Fairfax, VA 22030, USA
[3] LESIA, Observatoire de Paris, Université PSL, CNRS, Sorbonne Université, Univ. Paris Diderot, Sorbonne Paris Cité, 5 place Jules Janssen, F-92195 Meudon, France
[4] Konkoly Observatory, Research Centre for Astronomy and Earth Sciences, Hungarian Academy of Sciences, Konkoly Thege út 15-17., H-1121, Budapest, Hungary
[5] Space Science Division, Naval Research Laboratory, Code 7684, Washington, DC 20375, USA
Received 2020 November 30; revised 2021 February 16; accepted 2021 February 18; published 2021 April 19

Abstract

We analyze the coronal elemental abundances during a small flare using Hinode/EIS observations. Compared to the preflare elemental abundances, we observed a strong increase in coronal abundance of Ca XIV 193.84 Å, an emission line with low first ionization potential (FIP < 10 eV), as quantified by the ratio Ca/Ar during the flare. This is in contrast to the unchanged abundance ratio observed using Si X 258.38 Å/S X 264.23 Å. We propose two different mechanisms to explain the different composition results. First, the small flare-induced heating could have ionized S, but not the noble gas Ar, so that the flare-driven Alfvén waves brought up Si, S, and Ca in tandem via the ponderomotive force which acts on ions. Second, the location of the flare in strong magnetic fields between two sunspots may suggest fractionation occurred in the low chromosphere, where the background gas is neutral H. In this region, high-FIP S could behave more like a low-FIP than a high-FIP element. The physical interpretations proposed generate new insights into the evolution of plasma abundances in the solar atmosphere during flaring, and suggests that current models must be updated to reflect dynamic rather than just static scenarios.

Unified Astronomy Thesaurus concepts: The Sun (1693); Solar physics (1476); Solar flares (1496); Solar abundances (1474)

1. Introduction

Composition of plasma in the solar corona is a tracer of the flow of plasma and energy from the solar interior. Different complex processes such as the propagation and absorption of waves, convection of hot plasma, and reconnection and reconfiguration of magnetic fields can affect the flow and composition of plasma. This produces a clear and observable variation in the elemental abundances of coronal plasma across different regions of the solar atmosphere (e.g., Brooks et al. 2015).

In order to parameterize and study the coronal elemental abundances, we use the first ionization potential (FIP) bias, defined as taking the ratio of an element's coronal to photospheric abundance with respect to H. The FIP bias varies from solar structure to solar structure, and is closely linked to the Sun's magnetic field on all scales. Observed changes in elemental abundances take place on timescales of years (solar cycle), days or hours (magnetic flux emergence and decay), or minutes (flare) (Warren 2014; Brooks et al. 2017; Baker et al. 2018). In a quintessential active region, low-FIP elements (FIP < 10 eV) such as Ca, Mg, and Si exhibit enhanced abundances, while high-FIP elements (FIP ⩾ 10 eV) such as Ar, O, and S retain their photospheric abundances. This elemental fractionation is known as the FIP effect. The FIP bias of the photosphere is typically measured to be 1, with higher FIP bias values of 3–4 found in the closed loops of a developed active region (see Baker et al. 2013, 2015, 2018; Del Zanna & Mason 2014). The FIP bias value of quiet-Sun (Warren 1999; Baker et al. 2013; Ko et al. 2016) and coronal-hole regions (Feldman et al. 1998; Brooks & Warren 2011; Baker et al. 2013) has been explored extensively, and has also been used to link solar wind back to its source regions (Gloeckler & Geiss 1989; Fu et al. 2017).

In addition to the small magnetic perturbations that are common in a typical active region, rapid changes in magnetic connectivity can also contribute to a change in coronal composition. One of the events that causes rapid coronal composition changes is a solar flare. Solar flares are spectacular results of solar magnetic reconnection, characterized by the sudden release of energy and plasma. This rapid change of magnetic configuration triggers waves and energy that propagate into the chromosphere (Fletcher & Hudson 2008), followed by the ablation of plasma into the corona (Warren 2014). This produces the variability in coronal emission intensities observed by spectrometers. The standard and static coronal composition picture relies on a selective mechanism, generating a coronal composition that is different from the photospheric one. On the other hand, ablation does not act on specific elements. Warren (2014) studied 21 M- and X-class flares using the Solar Dynamics Observatory/EUV Variability Experiment (SDO/EVE) and showed that ablation acted on all elements and turned the Sun-as-a-star coronal elemental abundances temporarily closer to photospheric, in agreement with earlier results of Veck & Parkinson (1981), Feldman & Widing (1990), McKenzie & Feldman (1992), and Del Zanna & Woods (2013). However, an explanation that only comprises of ablation falls short on addressing some observations that obtained an enhanced low-FIP elemental abundances (e.g., Doschek et al. 1985; Sterling et al. 1993; Bentley et al. 1997; Fludra & Schmelz 1999; Phillips et al. 2010; Phillips & Dennis 2012; Dennis et al. 2015; Sylwester et al. 2015), as well as the more recent observations that have found evidence of an inverse FIP (IFIP) effect during different phases of flares

occurring in very complex active regions (Doschek et al. 2015; Doschek & Warren 2016; Baker et al. 2019, 2020; Katsuda et al. 2020).

So far, the only theoretical model that is able to explain both the FIP and IFIP effects is the ponderomotive force fractionation model, proposed by Laming (2004, 2009, 2011, 2015). In this model, FIP-effect fractionation is caused by the reflection and refraction of Alfvén waves in the upper chromosphere, especially in regions with high density gradients. The change in wave direction exerts a back reaction on the plasma ions, the ponderomotive force, and depending on the origin and nature of the waves this can vary in magnitude and sign. The direction of the ponderomotive force leads to ions that are guided in different directions, causing the FIP/IFIP effect.

In this paper, we present Hinode/Extreme-ultraviolet Imaging Spectrometer (Hinode/EIS) observations taken during a solar flare which originated in a reconnecting X-shaped structure rooted in a complex active region. EIS catching the flare in action provides an insight into the rapid evolution of solar coronal composition. The observations are presented in Section 2, with results and discussion in Sections 3 and 4. Conclusions are then discussed in Section 5.

2. Observations and Data Analysis

AR 11967 was an old and complex active region with a rich history. It was visible on the southern hemisphere of the Sun from 2014 January 31 to 2014 February 7. The active region was in its second rotation on disk, and major flux emergence and reconnection could be observed during this rotation. Figure 1 shows the magnetic complexity of AR 11967 from the SDO/Helioseismic and Magnetic Imager (HMI; Hoeksema et al. 2014) line-of-sight magnetic field data. Its complex and active nature led to numerous eruptions, resulting in 28 M-class flares and 83 C-class flares.

AR 11967 was particularly interesting as it hosted a very stable, long-lived X-shaped structure (previously identified and discussed by Liu et al. 2016; Jiang et al. 2017; Kawabata et al. 2017; Xue et al. 2017; Yang et al. 2017). This structure was observed from 2014 February 2–5, and was located between the sunspots S1 and S3 shown in the HMI magnetogram in Figure 1.

2.1. Coronal EUV and Magnetic Field Observations

The active region could be identified and studied on its evolution across the disk using the full-disk extreme-ultraviolet (EUV) and line-of-sight magnetogram images from the Atmospheric Imaging Assembly (AIA; Lemen et al. 2012) and the HMI instruments on board the SDO (Pesnell et al. 2012) spacecraft. Three different passbands from AIA were used in this analysis; 94 Å, 193 Å, and 131 Å. Images from the 193 Å passband are especially useful for FIP bias analysis as they capture emission from elements at around the same temperatures as one of the FIP bias pairs, Si X (258.38 Å) and S X (264.23 Å), formed at ∼1.25–1.5 MK. In contrast, 131 Å images are used as context images, as this passband benefits from clear flaring illumination, while 94 Å images were used to create the averaged intensity light curve. The HMI line-of-sight magnetic field images were used to demonstrate the magnetic evolution and flux emergence of the active region. Both the AIA and HMI data were processed using the standard aia_prep.pro routine within SolarSoftWare (Freeland & Handy 1998). This accounts for the differences in the plate scales and roll angles between AIA and HMI and correctly aligns the two instruments. Both 193 Å and 131 Å broadband images were also sharpened using the multiscale Gaussian normalization technique (MGN; Morgan & Druckmüller 2014).

2.2. EUV Spectroscopic Observations

The elemental abundance results discussed here were derived using spectroscopic observations from the EIS (Culhane et al. 2007) on board the Hinode spacecraft (Kosugi et al. 2007). Hinode/EIS observed AR 11967 on 2014 February 2, making three observations using two active region studies, study acronym HPW021_VEL_240x512v1 and Atlas_30 (study numbers 437 and 403, respectively). Table 1 shows the key details of the studies that were used to track the evolution of AR 11967. Study 437 has a large field of view of $240'' \times 520''$. It uses the slit scanning mode with the $1''$ slit and $1''$ scan step size, with a long exposure time of 60 s at each step for a total rastering time of 2 hr. In contrast, study 403 is a full CCD study, which has a smaller field of view of $120'' \times 160''$, using a $2''$ slit with a $2''$ step. At each pointing position, EIS exposed for 30 s to produce a raster with a duration of 30 minutes. Similar to the SDO data, the EIS data were preprocessed using the standard eis_prep.pro routine available in SolarSoftWare; this accounts for dark current, CCD bias, cosmic rays, hot, warm, dusty pixels, the radiometric calibration, and orbital correction. The eis_ccd_offset.pro routine was then used to ensure spatial consistency between different EIS spectral windows. The two pairs of low-FIP/high-FIP elements presented here are close in wavelength, however the Fe lines used for differential emission measure (DEM) span both EIS CCDs, so the Del Zanna (2013) Hinode/EIS calibration was used to calibrate the EIS data. In order to minimize the offset between Hinode/EIS and SDO, the intensity map of Fe XII 195.12 Å was aligned by eye using the AIA 193 Å passband. Since EIS Fe XII 195.12 Å and AIA 193 Å sample plasma from similar temperatures, the same solar structures could be identified in both maps, making instrumental alignment easier and more accurate.

2.3. Composition Maps

In our FIP bias examination, two pairs of emission lines, Si X 258.38 Å/S X 264.23 Å and Ca XIV 193.87 Å/Ar XIV 194.40 Å, were used extensively to examine composition measurements at two different solar atmospheric temperatures. Both pairs of elements are comprised of one low-FIP element, Si (Ca) and a high-FIP element, S (Ar).

2.3.1. Si X/S X Composition Map

The Si X (258.38 Å, FIP = 8.15 eV) and S X (264.23 Å, FIP = 10.36 eV) line pair has a comparably lower formation temperature at around 1.25–1.5 MK. The emissions from the consecutive ionization stages of Fe VIII–Fe XVI were fitted with a single Gaussian function, with the exception of Fe XI, Fe XII, and Fe XIII, which were fitted with multiple Gaussians to obtain their intensities. The effects of density variation were estimated using the fitted Fe XIII 202.04 Å/203.83 Å line-pair ratio. These intensities were then used to derive the DEM so that we can account for temperature effects when modeling the S X line intensity. Since the Fe lines lie on the short-wavelength detector and the Si and S lines lie on the long-wavelength

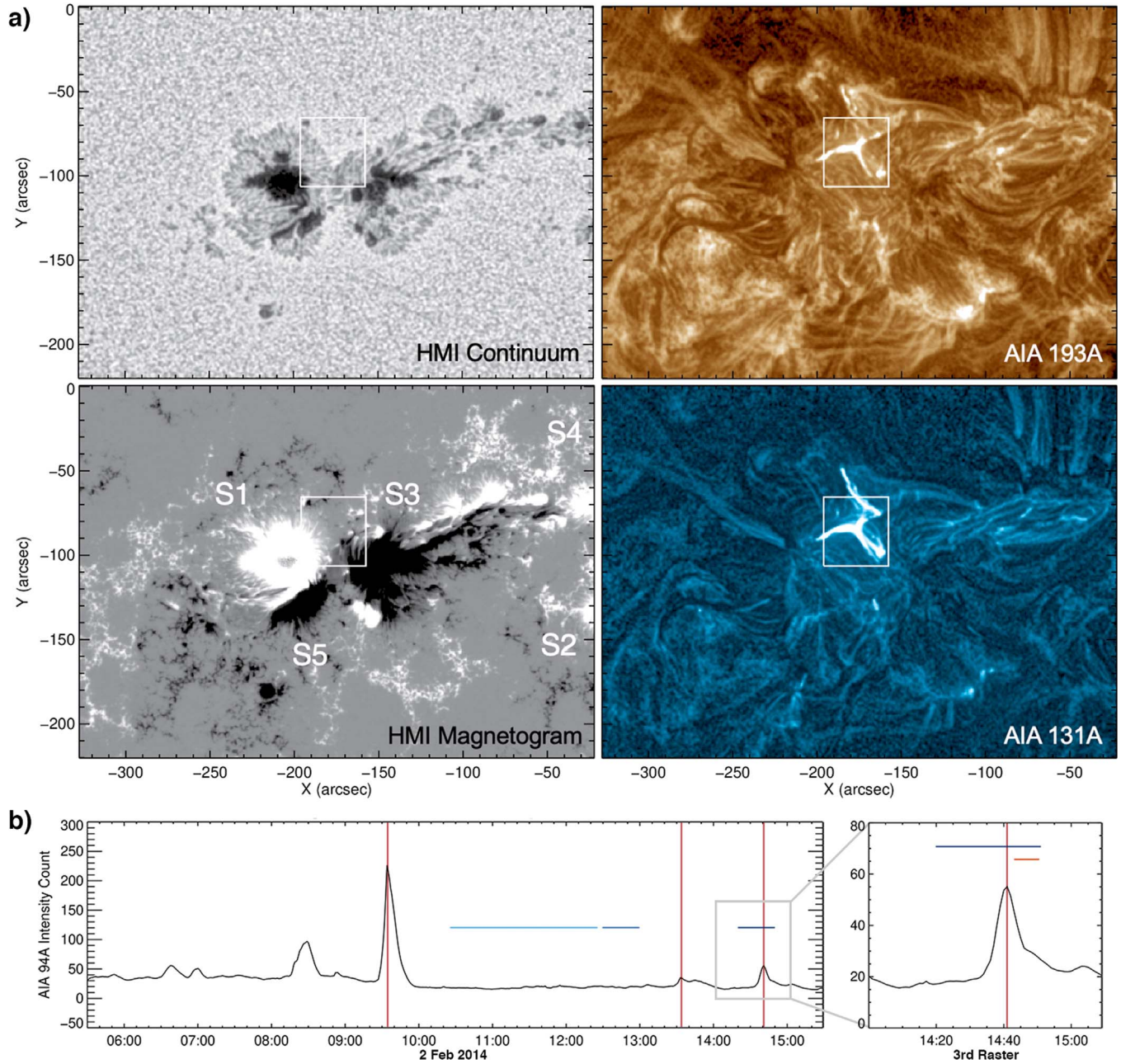

Figure 1. (a) HMI continuum; HMI magnetogram; AIA 193 Å; AIA 131 Å image during the flare at 14:34 UT on 2014 February 2. The white box indicates the EIS field of view in Figure 3. (b) AIA 94 Å light curve obtained using a 34″ × 31″ box surrounding the X-shaped structure in AR 11967. Blue horizontal lines indicate EIS rastering time and duration; red vertical lines indicate the flare time. The orange horizontal line in the zoomed section of the light curve indicates the EIS scan time over the X-shaped structure. The third flare happened during the third EIS raster, and EIS observed the X-shaped structure during its decay phase, roughly 1 minute after the peak of the flare.

detector, the emission measure was scaled to reproduce the intensity of Si X 258.38 Å. The CHIANTI Atomic Database, version 8.0 (Dere et al. 1997; Del Zanna et al. 2015) was used to obtain the contribution functions, applying the photospheric abundances of Grevesse et al. (2007) for all the spectral lines, while assuming the Fe XIII density calculated above. Lastly, both Si X 258.38 Å and S X 264.23 Å, which form our FIP bias ratio, were fitted with a single Gaussian function. The Markov Chain Monte Carlo (MCMC) algorithm from the PINTofALE software package was used to compute the emission measure distribution for the Fe lines (Kashyap & Drake 2000). The emission measure distribution was then convolved with the CHIANTI contribution functions and fitted to the observed spectral intensity of the low-FIP Fe emission lines. Since both Fe and Si are low-FIP elements, the best-fit emission measure for each pixel will be enhanced by some factor due to the FIP effect. We can determine this factor by calculating the intensity of the S X 264.23 Å line; assuming S is a high-FIP element that is not enhanced. Finally, the Si/S FIP bias ratio presented in this paper is then the ratio of the predicted to observed intensity of the S X 264.23 Å line. In total, 17 spectral lines were used to infer our Si X 258.38 Å/S X 264.23 Å composition maps. Data pixels with a $\bar{\chi}^2 > 17$ were discarded during our analysis. Since EIS is formed by both short-wavelength and long-wavelength detectors with an offset of 18.5 pixels in the y direction, part of our region of interest that lies at the top of the

Table 1
Hinode/EIS Study Details Used in This Study

Study Number	437
Study Acronym	HPW021_VEL_240x512v1
Emission Lines	Fe VIII 185.213 Å, Fe VIII 186.601 Å Fe IX 188.497 Å, Fe IX 197.862 Å Fe X 184.536 Å, Fe XI 188.216 Å Fe XII 192.394 Å, Fe XII 195.119 Å Fe XIII 202.044 Å, Fe XIII 203.826 Å Fe XIV 264.787 Å, Fe XIV 270.519 Å Fe XV 284.16 Å, Fe XVI 262.984 Å Fe XVII 254.870 Å Si X 258.38 Å, S X 264.23 Å Ca XIV 193.87 Å, Ar XIV 194.40 Å
Field of View	240″ × 512″
Rastering	1″ slit, 120 positions, 2″ coarse steps
Exposure Time	60 s
Total Raster Time	2 hr
Reference Spectral Window	Fe XII 195.12 Å
Study Number	403
Study Acronym	Atlas_30
Emission Lines	Si X 258.38 Å, S X 264.23 Å Ca XIV 193.87 Å, Ar XIV 194.40 Å
Field of View	120″ × 160″
Rastering	2″ slit, 60 positions, 2″ steps
Exposure Time	30 s
Total Raster Time	30 minutes
Reference Spectral Window	Fe XII 195.12 Å

long-wavelength detector was not captured by the short-wavelength detector. The lack of data for the Si X 258.38 Å/S X 264.23 Å composition calculation contributed to a horizontal strip of data with very high $\bar{\chi}^2$ value, and this resulted in the patch of missing data shown in Figure 3. The estimated uncertainty of the Si X 258.38 Å/S X 264.23 Å FIP bias ratio is 0.30, assuming a 20% spectral line intensity error. This approach is discussed in detail by Brooks et al. (2015), and is designed to remove the temperature and density effects for a robust calculation of the FIP bias in different solar features.

2.3.2. Ca XIV/Ar XIV Composition Map

The Ca XIV (193.87 Å, FIP = 6.11 eV) and Ar XIV (194.40 Å, FIP = 15.76 eV) emission lines are formed at a comparably higher ionization equilibrium temperature of around 3.5 MK ($\log_{10}T = 6.55$) (Feldman et al. 2009). Both lines are relatively strong and present similar emissivity temperature dependence. Three Gaussian functions were fitted to both the Ca XIV 193.87 Å and Ar XIV 194.40 Å lines, as Ca XIV 193.87 Å is sandwiched between two other lines, and sometimes Ar XIV is blended with two very faint lines along its blue wing (Brown et al. 2008). In this paper, we follow the analysis done by Doschek et al. (2015), Doschek & Warren (2016, 2017), Baker et al. (2019, 2020) in producing the composition maps. In particular, Doschek & Warren (2017) describes the assumptions and issues that come with this composition diagnostic. We used $\log_{10}$ abundance values relative to $\log_{10}H$ as: coronal Ca = 6.93 (Feldman 1992), photospheric Ca = 6.33 (Lodders et al. 2009), and coronal and photospheric Ar = 6.50 (Lodders et al. 2009). Since the spectral intensity of Ar at the photosphere could not be directly measured, its abundance value (photospheric Ar) is determined indirectly through spectra observed in solar wind, solar flares, or solar energetic particles. As a result, there has historically been a relatively large fluctuation of the photospheric Ar abundances. Figure 2 shows a plot of the ratio of Ca XIV 193.87 Å to Ar XIV 194.40 Å contribution functions at various densities using the abundances above. This yields a typical coronal active region FIP bias of 4 and has the advantage of being quick and simple. However, taking the ratio between the low-FIP Ca XIV 193.87 Å to the high-FIP Ar XIV 194.40 Å does not account for the effects of temperature and density. To alleviate the concerns over the ratio value being sensitive to these effects, temperatures were calculated using the ratio between Ca XV 200.97 Å and Ca XIV 193.87 Å around the region of interest; its temperature histogram is also shown in Figure 2. The Ca/Ar composition maps observed before and during the flare are similar in temperature at $\sim\log_{10}T = 6.65$K. The range of electron temperatures during the flare was also narrow, and ranges between $\log_{10}6.59$–$\log_{10}6.68$. When these two pieces of evidence are put side by side with the significant intensity ratio changes observed across the Ca/Ar maps, the temperature and density can be seen to have a minimal effect for our analysis. The contribution functions that are convolved with the DEM at the flaring region are shown in the Appendix.

2.4. Region Definition

In Figure 3, we can observe a significant increase in the Ca/Ar intensity ratio value in our third raster (panel (f)) corresponding to the stable structure, which clearly describes its X-shaped morphology. Since this X-shaped structure is extremely stable throughout the period studied here on 2014 February 2, we defined the flaring region using pixels with an intensity ratio value >3 in this raster. This intensity ratio value represents an enhanced FIP bias. The pixels corresponding to this region of interest were then differentially rotated to the times of the two previous rasters on 2014 February 2, at 10:25 UT and 12:29 UT. The white border in each panel of Figure 3 shows the extent of this region of interest differentially rotated to the corresponding raster time. In each case there is good agreement, indicating the stability of the X-shaped structure and the robust nature of the method used to define the region of interest.

3. Results

Although the active region was observed by EIS between 2014 February 1 and 5, and the X-shaped structure was apparent between February 2 and 4, here we focus on its evolution between 9:30 UT and 14:50 UT on February 2. The bottom panel of Figure 1 shows the averaged intensity in the 94 Å passband in the field of view shown by the white box in Figure 1(a). Multiple brightenings can be identified, with the three blue horizontal lines indicating the periods of the EIS rasters. The first flare was the strongest, starting at 09:26 UT, ~1 hr before the start time of our first raster. It peaked at 09:35 UT, and decayed to background intensity levels by ~09:51 UT. The second flare was a very minor flare as shown by the small peak in Figure 3. It started at 13:22 UT, after our first two rasters and around 1 hr before the start time of our third raster. It peaked at 13:29 UT and decayed into background intensity levels by ~13:53 UT. Finally, the third flare took place during the third EIS raster described here. The flare started at 14:27 UT, approximately 9 minutes into the raster, peaked at 14:37 UT and decayed to background intensity level

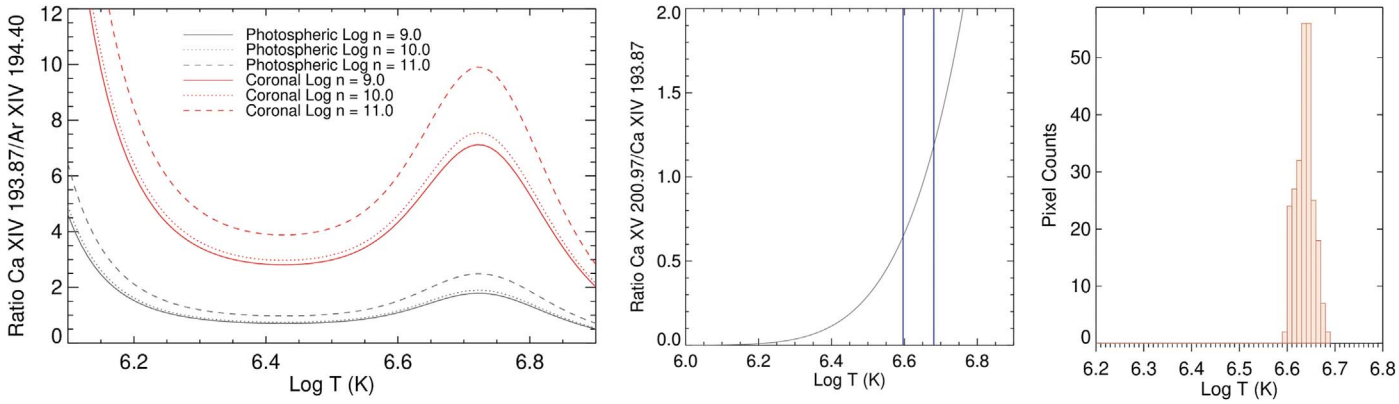

Figure 2. Left to right: (a) intensity ratio of Ca XIV 193.87 Å and Ar XIV 194.40 Å contribution function with respect to electron temperature for electron density of $\log_{10} N = 9.0$, 10.0, 11.0; (b) intensity ratio of Ca XV 200.97 Å and Ca XIV 193.87 Å contribution function with respect to electron temperature; (c) temperature histogram around the flaring region.

by ∼14:56 UT. Neither flare 2 or 3 could be identified in the Geostationary Operational Environmental Satellite's (GOES) X-ray flux, indicating that they were very minor flares.

3.1. Magnetic Field Evolution

AR 11967 was a highly complex AR built up by at least three major bipoles in various stages of their evolution. Figure 1 shows both S1 and S2, which were leading (positive) polarity spots produced by two flux emergence episodes before the AR rotated onto the disk. We can see that the negative S5 is located tightly below S1, but in fact S1 and S2's following (negative) polarities had already dispersed by this time. Despite this, S1 was still a large spot exceeding 100 MSH according to the Debrecen Photoheliographic Data. A major flux emergence occurred in the AR during the EIS observation period, with its principal spots being S4 (positive) and S3 (negative) in Figure 1. The parallel strands of opposite polarities in between S4 and S3 indicate that this emerging bipole is strongly sheared. The magnetic polarity pattern (magnetic tongues, see Luoni et al. 2011) is indicative of negative, left-handed twist. As S4 and S3 are separating in the course of flux emergence, the negative polarity S3 is moving toward the positive polarity S1. As the flare observed with EIS took place in between spots S3 and S1 (see Figure 1), a forcing by their persistent approach was creating strong field gradients in the proximity of the X-shaped structure (Jiang et al. 2017; Kawabata et al. 2017).

3.2. Enhanced Low-FIP Elemental Abundances of the Third Flare

Figure 3 shows the Si X/S X composition map and the Ca XIV/Ar XIV intensity ratio map from the three EIS rasters made on 2014 February 2. EIS made two raster observations after the first flare, with the second flare occurring before, and the third flare during, the third EIS raster. It can be seen in the first row of Figure 3 that, across the three observations, in a temperature range ∼1.25–1.5 MK, the Si X/S X composition map does not show drastic changes, and the map is generally red/dark orange in color, comparable to a composition map of a quiet-Sun region or a small active region.

However, at a higher temperature (corresponding to the Ca XIV/Ar XIV ratio maps), a significant enhancement in FIP bias can be observed during the third flare. For the first two rasters, the region of the solar flare shows up as red in the intensity ratio map, indicating an ordinary quiet-Sun FIP bias value of 2, similar to the FIP bias value calculated using the Si X/S X composition map. However, a clear change in coronal abundances can be seen in the third raster, where EIS observes the third flare (as a yellow region, indicating enhanced FIP) which peaked at 14:29 UT. The shape of the enhanced intensity ratio patch fully traces the topology of the X-shaped flare structure.

These changes in the maps are reflected in the data histograms in Figure 4 taken around the flaring region. The Si X/S X histogram shows little change between the three observations. On the other hand, the Ca XIV/Ar XIV ratio value histogram shows a drastic enhancement in the mean FIP bias value, which changes from a quiet-Sun value of ∼2 to 3.77, which is well beyond the estimated error. The FIP bias value therefore exhibits a significant difference between two different temperatures.

4. Discussion and Interpretation

In this study, we have analyzed the instantaneous coronal plasma evolution of a small flare in a reconnecting X-shaped structure located in the highly active AR 11967 observed by Hinode/EIS on 2014 February 2. This opened up a possibility of obtaining composition during a solar flare. Over the course of the three observations, a low-FIP bias value of ∼2 can be seen across all of the Si/S composition maps. Although the higher temperature Ca/Ar composition map shows comparable behavior for the first two rasters, it shows a significantly enhanced ratio value for the third raster in both the composition map and the ratio value histogram in Figure 4, indicating a strong FIP effect during the flare. This inconsistent behavior between composition maps formed using two line pairs is very interesting as it is different from the photospheric composition in flares found by Warren (2014) and Baker et al. (2019), which is typically interpreted as an enhancement of photospheric material in the corona due to chromospheric ablation as part of the flare process.

4.1. Physical Interpretation

We suggest two possible scenarios that could help to explain the evolution of the composition, in addition to the ablation picture we expect after flares. First, the fact that S as a high-FIP element has a relatively low-FIP value which is close to 10 eV. Second, the potential shift of elemental fractionation height due to the strong magnetic fields observed here.

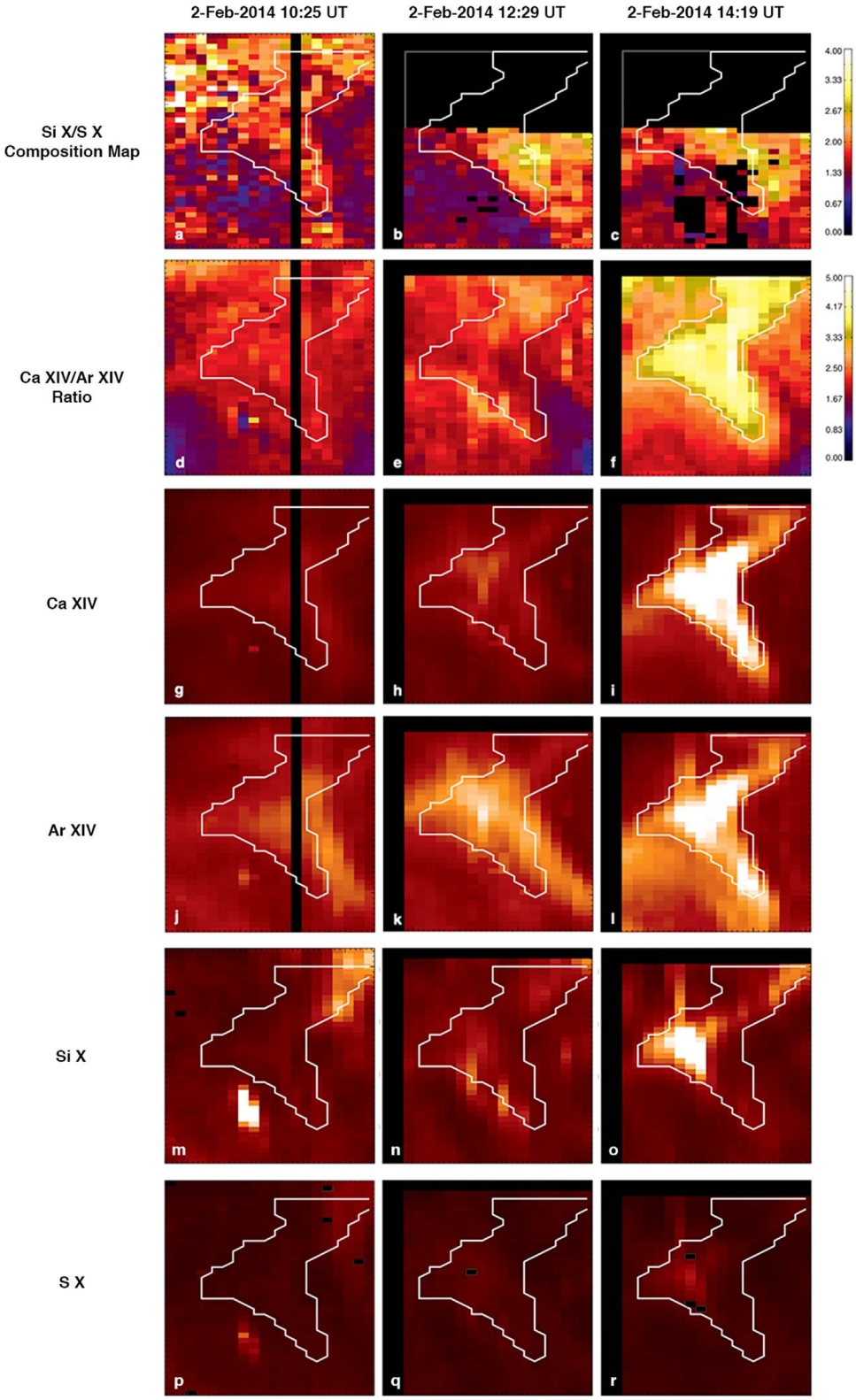

Figure 3. Top to bottom: Hinode/EIS Si X 258.38 Å/S X 264.23 Å composition map, Ca XIV 193.87 Å/Ar XIV 194.40 Å intensity ratio maps, Ca XIV 193.87 Å intensity maps, Ar XIV 194.40 Å intensity maps, Si X 258.38 Å intensity maps and S X 264.23 Å intensity maps. The contour indicates the flaring region used for analysis. Left to right: observations from three different EIS spectral scans on 2014 February 2, starting at 10:25 UT, 12:29 UT, and 14:19 UT, respectively. In the composition and intensity ratio maps, blue represents a photospheric-like (unenhanced composition) FIP bias of 1; red represents a quiet-Sun composition and yellow shows a high-FIP bias composition. A clear X shape of the structure could be observed in the 14:19 UT raster. The algorithm to calculate the Si X 258.38 Å/S X 264.23 Å composition map minimizes temperature and density effects by utilizing both the short-wavelength and long-wavelength detectors of Hinode/EIS. Offset between the two detectors contributed to the patch of dark pixels in the composition maps; the Ca XIV 193.87 Å/Ar XIV 194.40 Å ratio maps are simply the intensity ratio of the two spectral lines. A more detailed description can be found in Sections 2.3.1 and 2.3.2.

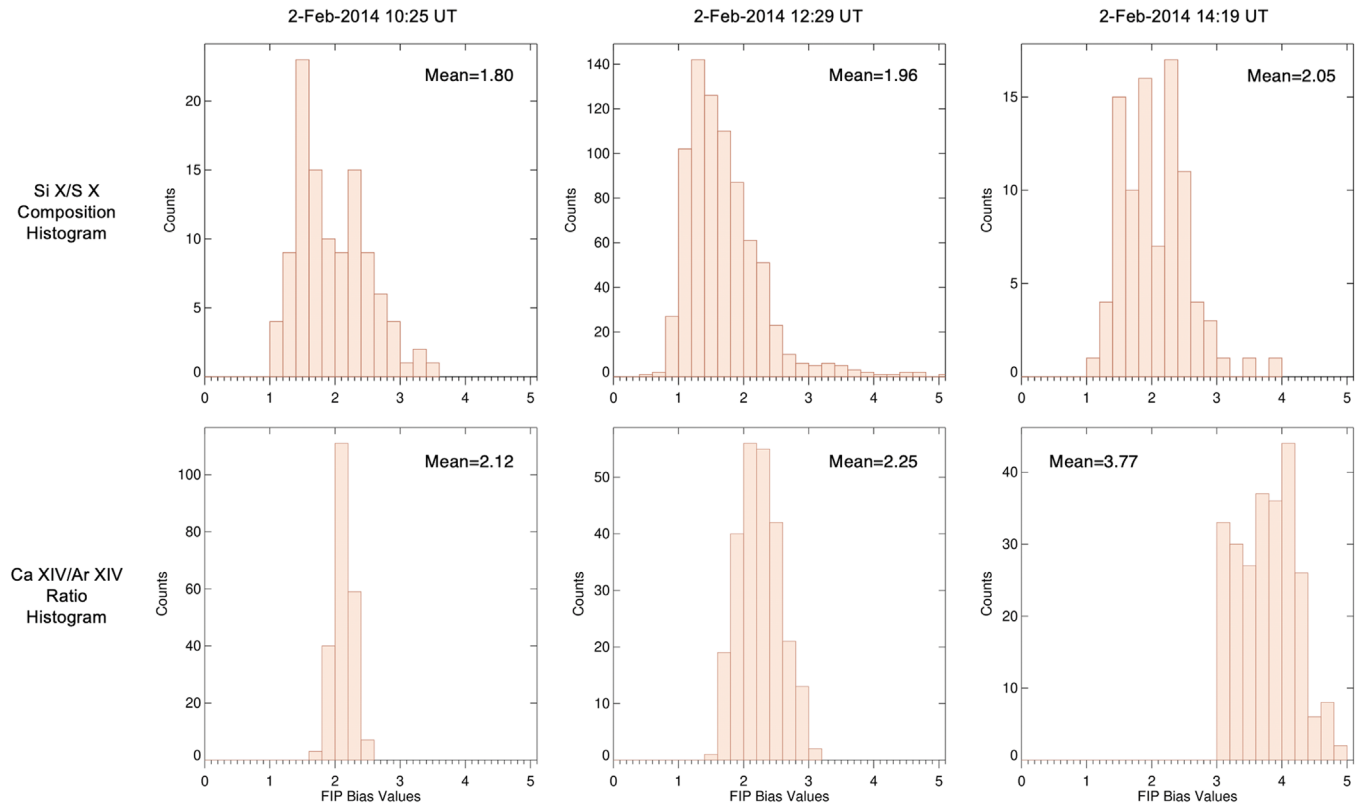

Figure 4. Top to bottom: histogram of (a) Si X 258.38 Å/S X 265.23 Å FIP bias values and (b) Ca XIV 193.87 Å/Ar XIV 194.40 Å intensity ratio values, at the region of interest highlighted with the white contour in Figure 3.

The model to explain the observed fractionation of elemental abundances in the solar atmosphere is a quasi-static model of long-lasting structures such as coronal loops, active regions and solar wind outflow regions (see Laming 2004; Laming et al. 2019). Under these static scenarios, in closed loops, the fractionation occurs at the top of the chromosphere. Warren (2014) studied the evolution of plasma composition in large flares which involves a dynamic rapid evolution of plasma parameters (highly time dependent), and suggested that in some dramatic time-dependent events like large M-and X-class flares, the observed elemental abundance variation was due to plasma ablated from deep in the chromosphere, below where fractionation occurs. However, this is not the case here, where an enhanced abundance of Ca, or in other studies, where an enhancement of other various low-FIP elements (e.g., Fludra & Schmelz 1999; Phillips et al. 2010; Phillips & Dennis 2012; Dennis et al. 2015) was observed. Therefore, we have to look for other mechanisms to find an explanation.

4.1.1. Partial Ionization of Different Elements

First, the different composition evolution in the Si/S and Ca/Ar line pairs could be due to the actual FIP values of these elements. We have adopted the convention of categorizing Si and Ca as low-FIP elements and S and Ar as high-FIP elements. While S is typically categorized as a high-FIP element, it has a relatively low FIP value of 10.36 eV, whereas Si, typically categorized as a low-FIP element, has a comparable FIP value of 8.15 eV. The difference between their FIP values is therefore merely 2.21 eV. In contrast, as Ar is a noble gas, it has a much higher FIP of 15.76 eV, with the result that the difference in FIP between it and Ca (FIP = 6.11 eV) is 9.65 eV.

During a flare, magnetic reconnection produces Alfvén waves that travel from the corona to the chromosphere (e.g., Fletcher & Hudson 2008). The refraction of such waves at the top of the chromosphere can then create an upward ponderomotive force that acts only on ions (see Laming 2009). However, the same reconnection process also accelerates and heats particles, which at their impact onto the chromosphere lead to heating and consequent ablation of plasma. For fractionation to occur, the Alfvén speed must be greater than the electron thermal speed, so that following coronal energy release, Alfvén waves get to the chromosphere first to cause fractionation before the heat conduction flux arrives to cause the evaporation. If this is violated, unfractionated plasma will be evaporated into the flare loops. However, if the two speeds were about equal, fractionation with extra ionization of S would result. For the flare studied here, which was very small, the heating produced could have been sufficient to ionize S with its relatively low FIP, with the ponderomotive force bringing up both Si and S in tandem, thus maintaining the quiet-Sun FIP bias values that can be seen across the Si/S composition maps and their respective data histograms. On the contrary, due to the relatively high FIP of Ar, the small heating associated with the observed small flare was insufficient to ionize Ar. Instead, the more abundant low-FIP Ca ions were brought up by the ponderomotive force, thus generating the fractionation observed in the third Ca/Ar intensity ratio map.

Within the above interpretation, this observation could open up a unique way to probe into the fractionation height in the solar atmosphere by different solar phenomena. With the partial ionization of S but not Ar, one can estimate the upper

chromospheric temperature at the time of the flare. Using Laming et al. (2019), the chromospheric model by Avrett & Loeser (2008) and collisional ionization equilibrium calculation from Mazzotta et al. (1998), the chromospheric temperature needs to be

$$2.5 \times 10^4 \text{ K} < T < 3.0 \times 10^4 \text{ K}. \quad (1)$$

The true temperature is likely to be lower, because calculations from Mazzotta et al. (1998) neglect photoionization and density effects. Nonetheless, this postulation provides an additional insight into the work done by Warren (2014) and Dennis et al. (2015), who studied the composition evolution in large flares. For larger flares, more energy is released, which should produce a correspondingly large increase in temperature, thus ionizing Ar. This would then produce sufficient ionized Ar to experience the ponderomotive force, resulting in the photospheric-like coronal composition more commonly observed during flares.

4.1.2. Fractionation in the Low Chromosphere

Another plausible scenario comes from the fact that the flare studied here took place between the strong magnetic fields of two large sunspots. This has the effect of lowering the plasma $\beta = 1$ height and consequently the fractionation height of the different elements. As identified in Fletcher & Hudson (2008), a solar flare which triggers reconfiguration of the magnetic field generates large-scale Alfvén waves which propagate from the flaring site to the lower chromosphere, where the background gas is neutral H. In this region, high-FIP S behaves like a low-FIP element (Laming et al. 2019); behavior consistent with the statistically insignificant changes of Si/S FIP bias observed here. This requires a relaxing of the quasi-static nature of FIP models, to allow fractionation to occur throughout the chromosphere and not just at the top, which follows if the waves are in resonance with the loop. As with the scenario involving partial ionization described above, this would result in fractionation of Ca and both Si and S, producing the constant Si/S and an increase in Ca/Ar observed here. These observations are consistent with the ponderomotive force interpretation for variation in FIP bias.

4.2. AIA Wavelet Analysis

Although the two physical interpretations both seem plausible, they both rely on flare-driven downward traveling Alfvén waves which induce the ponderomotive force acting upwards. To try and identify this essential signature of Alfvén waves propagating to the chromosphere, the AIA data in different passbands were analyzed using a wavelet technique similar to that previously used by, e.g., Milligan et al. (2017) and Hayes et al. (2016). The intensity in the HMI continuum, 1600, 1700, 304, 131, and 94 Å passbands was averaged within the region indicated by the white box shown in Figure 1. The top left of Figure 5 shows the normalized wavelet analysis of the wavelengths, with the top right panel showing the detrended data produced by subtracting a smoothed version of the data. This was then analyzed using the wavelet technique of Torrence & Compo (1998). It can be seen in Figures 5(c)–(h) that each of the different passbands (with the exception of the HMI continuum) exhibits a variation in the signal associated with the small-scale brightening discussed here. However, the signals are in the form of a single peak instead of an oscillation. Moreover, in terms of the signal strength, apart from 304 Å, no other passbands show a significant intensity. It is also notable that most of the observed signal for each passband is below the white triangular lines, indicating that they are not statistically significant and are outside the zone of influence.

This suggests that the Alfvén waves produced by the flare in the corona proposed by Fletcher & Hudson (2008) could not be observed in the lower solar atmosphere using the data available here. The lack of a statistically sound signal that could support wave propagation is disappointing, but this result could still inform several investigation directions for future work. First, the instrument, AIA, used in the analysis has a relatively longer cadence of 12 s, which places a limit on the frequency of the observable signal. Using an instrument with a higher cadence, such as GOES's X-ray sensor could show the finer scale oscillations, albeit without the spatial resolution required here. A back of the envelope calculation gives insight into the wavelet period we can look into in the future, using a simple calculation from the coronal loop length and $v_A = B/\sqrt{\mu_0 \rho}$, where v_A is the Alfvén speed. In our case, taking from the observations and assuming a semicircular coronal loop, the loop length can be estimated to be $\sim 40''$, and the x-shaped structure is rooted in an intense magnetic field with a line-of-sight field strength of $\sim$2500 Gauss. Assuming a loop density of $\sim 3 \times 10^{-7}$ kg m^{-3} (Kohutova & Verwichte 2017), this gives the line-of-sight Alfvén speed, v_{Az}, to be $\sim$400 km s^{-1}, and a resonant wave period of 140 s. This value can then be compared with future wavelet analysis and help pinpoint the Alfvén waves.

Second, AIA is a broadband imager, which captures spectral lines across a wide range of ions. Although a strong signal can be found in the 304 Å wavelet analysis, which seems to suggest variations indeed exist in the chromosphere, the contributing spectral lines could not be precisely identified. The use of cotemporal narrowband spectroscopic data could provide more insight into the wave propagation depth, and perhaps open up the possibility of correlating the oscillation strength with the observed FIP bias.

5. Conclusions

In this paper we have presented observations of the highly complex active region, AR 11967, which have provided a unique opportunity to study the evolution of composition in a small flare that occurred between two large sunspots. On 2014 February 2, EIS observed a small flare within an X-shaped structure in the active region. The results show very different composition evolution at two different line pairs of different formation temperatures, with an unchanged composition obtained in the lower-temperature Si X/S X composition map in the flaring region, while a significant FIP bias value increase was observed in the higher-temperature Ca XIV/Ar XIV composition ratio.

We propose two possible physical interpretations which could explain or contribute to the strange composition evolution. First, in the case of partial ionization, due to the relatively low first ionization potential of S, both Si and S were ionized by the small third flare with relatively low chromospheric heating, leaving the Si X/S X FIP bias value unchanged. While the lower FIP of S meant that it could be ionized by the small flare observed here, the much higher FIP value of Ar meant that it could not be easily ionized. The

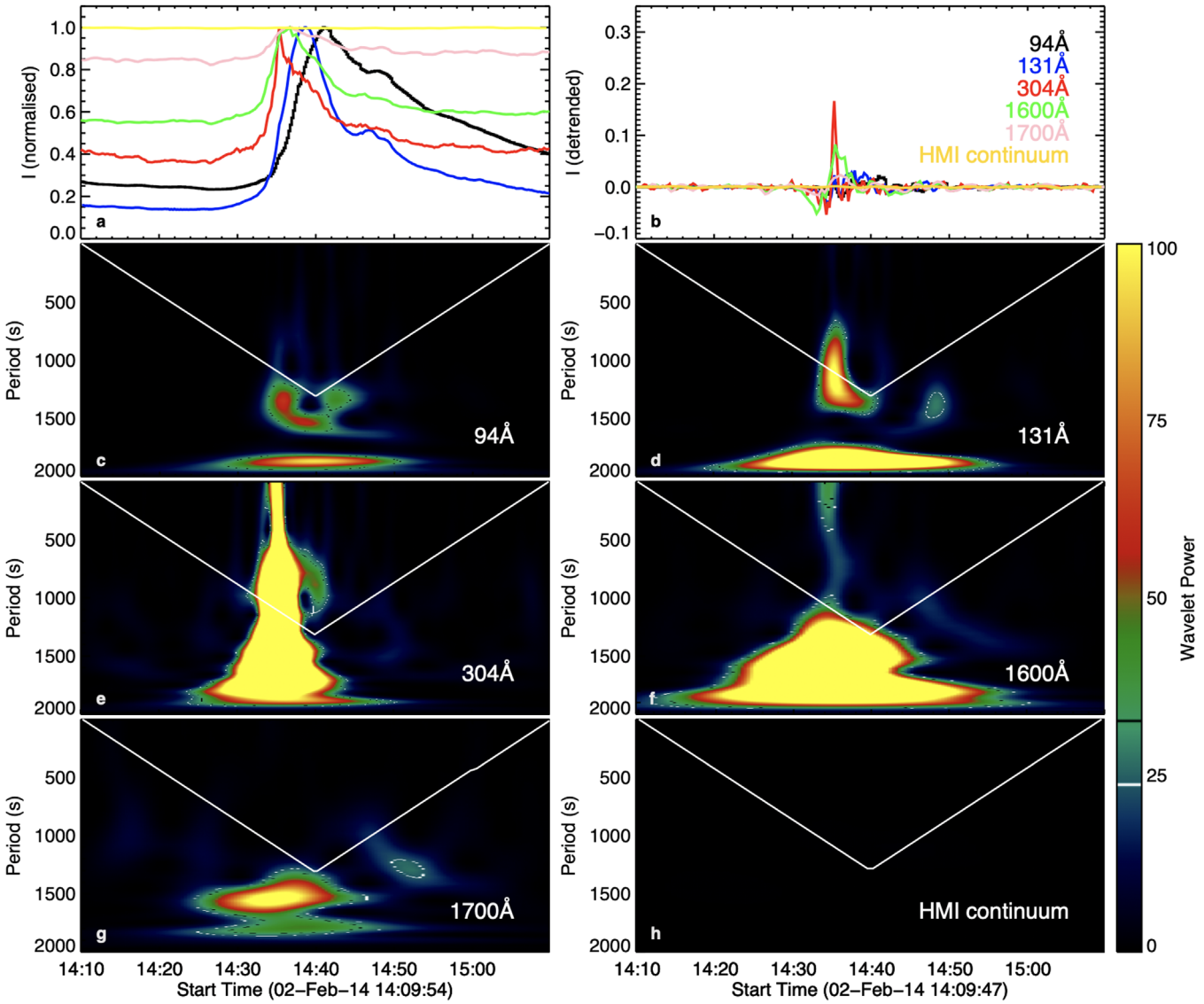

Figure 5. Wavelet analysis of AIA 94 Å, 131 Å, 304 Å, 1600 Å, 1700 Å, and HMI continuum during the third flare at 14:37 UT.

resulting ponderomotive force produced by the waves originating from magnetic reconnection leading to the flare thus only brought up the ionized Ca, Si, and S in tandem. A similar yet not mutually exclusive mechanism could be present in our second interpretation—fractionation at the lower chromosphere. Our flare occurred between two sunspots, rooted in a region of strong magnetic field. This has the effect of lowering the regions of fractionation of the different elements. Alfvén waves generated by the flare traveled to the lower chromosphere, where the background gas is neutral H. Under this condition, S behaves like a low-FIP element. Therefore both Si and S fractionate in this flare and the Si/S ratio does not change, while the high-FIP Ar does not change its behavior. This creates a significant discrepancy that can be observed between the two sets of composition maps. Both interpretations of the evolution of composition during a small flare that we present here are consistent with the ponderomotive force interpretation for variation in FIP bias.

Since these two interpretations involve Alfvén waves that travel to the chromosphere, a wavelet analysis approach applied to the cotemporal AIA data was used to search for wave signatures. However, waves in the lower chromosphere during the reconnection were not detected with this method. Nonetheless, this provides further investigation direction at correlating elemental fractionation with wave oscillations. First, the relatively long cadence of AIA (12 s) limits the observation of very high-frequency signals. Second, AIA/SDO is a broadband imager. Signals obtained from different passbands merely give a very arbitrary idea of the solar altitude. The use of a cotemporal narrowband spectrometer will give more insight of the wave propagation depth, and perhaps open up the possibility of correlating the oscillation strength with the observed FIP bias. Some of the work to combine observations between different layers of the solar atmosphere has been done in Baker et al. (2021) and Stangalini et al. (2021), using the Interferometric BIdimensional Spectrometer (IBIS), EIS, and magnetic field modeling. Ground-based instruments like IBIS and the Daniel K. Inouye Solar Telescope will be extremely valuable in the future, by directly observing where the wave refraction and reflections are proposed to happen. The upcoming Solar-C EUV High-Throughput Spectroscopic Telescope (EUVST) and its wide range of temperature coverage can

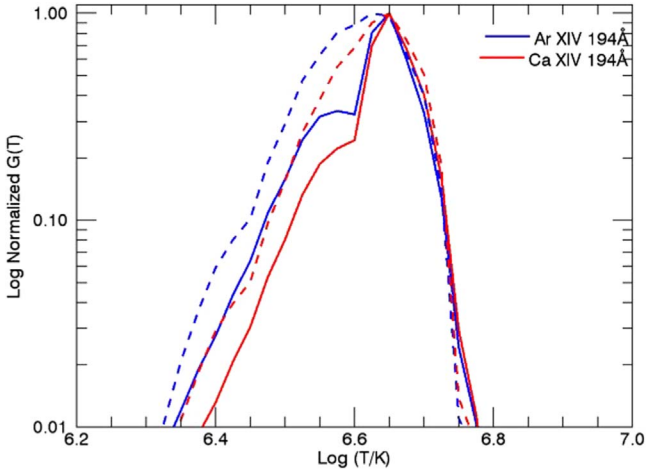

Figure 6. Log normalized contribution functions, G(T) of Ca XIV 193.87 Å and Ar XIV 194.40 Å convolved with the DEM for the flaring region. Dashed lines represent DEMs calculated from the 12:29 UT raster; solid lines were calculated using the 14:19 UT (flaring) raster.

also contribute massively by observing different layers of our Sun's atmosphere simultaneously. If the existence of Alfvén waves can be confirmed, this observation could be the another step to understand the physical mechanism behind composition evolution during flares, and current theories need to factor the time evolution of composition into their modeling.

A.S.H.T. thanks the STFC for support via funding given in his PhD studentship. D.M.L. is grateful to the Science Technology and Facilities Council for the award of an Ernest Rutherford Fellowship (ST/R003246/1). The work of D.H.B. was performed under contract to the Naval Research Laboratory and was funded by the NASA Hinode program. D.B. is funded under STFC consolidated grant No. ST/S000240/1 and L.v.D.G. is partially funded under the same grant. L.v.D.G. acknowledges the Hungarian National Research, Development and Innovation Office grant OTKA K-131508. J.M.L. was supported by the NASA Heliophysics Guest Investigator (80HQTR19T0029) and Supporting Research (80HQTR20T0076) programs, and by Basic Research Funds of the Office of Naval Research. G.V. acknowledges the support from the European Union's Horizon 2020 research and innovation program under grant agreement No. 824135 and of the STFC grant number ST/T000317/1. Hinode is a Japanese mission developed and launched by ISAS/JAXA, with NAOJ as domestic partner and NASA and STFC (UK) as international partners. It is operated by these agencies in cooperation with ESA and NSC (Norway). AIA data courtesy of NASA/SDO and the AIA, EVE, and HMI science teams. CHIANTI is a collaborative project involving George Mason University, the University of Michigan (USA), and the University of Cambridge (UK).

Appendix

In this section, we address the concern of the temperature effect on the Ca XIV/Ar XIV intensity ratio value. In Figure 2, the electron temperature at the flaring region ranges from $\log_{10} 6.59$–$\log_{10} 6.68$. This puts the theoretical intensity ratio at the uphill region in Figure 2(a), suggesting that a change in temperature could produce the observed change in the intensity ratio. Figure 6 shows the differential emission measure~(DEM) performed around the region of interest. Over the temperature range, two curves coincide very well, and the peak temperature does not change significantly, suggesting the dramatic increase in intensity ratio value is real.

ORCID iDs

Andy S. H. To https://orcid.org/0000-0003-0774-9084
David M. Long https://orcid.org/0000-0003-3137-0277
Deborah Baker https://orcid.org/0000-0002-0665-2355
David H. Brooks https://orcid.org/0000-0002-2189-9313
Lidia van Driel-Gesztelyi https://orcid.org/0000-0002-2943-5978
J. Martin Laming https://orcid.org/0000-0002-3362-7040
Gherardo Valori https://orcid.org/0000-0001-7809-0067

References

Avrett, E. H., & Loeser, R. 2008, ApJS, 175, 229
Baker, D., Brooks, D. H., Démoulin, P., et al. 2013, ApJ, 778, 69
Baker, D., Brooks, D. H., Démoulin, P., et al. 2015, ApJ, 802, 104
Baker, D., Brooks, D. H., van Driel-Gesztelyi, L., et al. 2018, ApJ, 856, 71
Baker, D., Stangalini, M., Valori, G., et al. 2021, ApJ, 907, 16
Baker, D., van Driel-Gesztelyi, L., Brooks, D. H., et al. 2019, ApJ, 875, 35
Baker, D., van Driel-Gesztelyi, L., Brooks, D. H., et al. 2020, ApJ, 894, 35
Bentley, R. D., Sylwester, J., & Lemen, J. R. 1997, AdSpR, 20, 2275
Brooks, D. H., Baker, D., Van Driel-Gesztelyi, L., & Warren, H. P. 2017, NatCo, 8, 1
Brooks, D. H., Ugarte-Urra, I., & Warren, H. P. 2015, NatCo, 6, 5947
Brooks, D. H., & Warren, H. P. 2011, ApJL, 727, L13
Brown, C. M., Feldman, U., Seely, J. F., Korendyke, C. M., & Hara, H. 2008, ApJS, 176, 511
Culhane, J. L., Harra, L. K., James, A. M., et al. 2007, SoPh, 243, 19
Del Zanna, G. 2013, A&A, 555, A47
Del Zanna, G., Dere, K. P., Young, P. R., Landi, E., & Mason, H. E. 2015, A&A, 582, A56
Del Zanna, G., & Mason, H. E. 2014, A&A, 565, A14
Del Zanna, G., & Woods, T. N. 2013, A&A, 555, A59
Dennis, B. R., Phillips, K. J. H., Schwartz, R. A., et al. 2015, ApJ, 803, 67
Dere, K. P., Landi, E., Mason, H. E., Fossi, B. C. M., & Young, P. R. 1997, A&AS, 125, 149
Doschek, G. A., Feldman, U., & Seely, J. F. 1985, MNRAS, 217, 317
Doschek, G. A., & Warren, H. P. 2016, ApJ, 825, 36
Doschek, G. A., & Warren, H. P. 2017, ApJ, 844, 52
Doschek, G. A., Warren, H. P., & Feldman, U. 2015, ApJL, 808, L7
Feldman, U. 1992, PhyS, 46, 202
Feldman, U., Schühle, U., Widing, K. G., & Laming, J. M. 1998, ApJ, 505, 999
Feldman, U., Warren, H. P., Brown, C. M., & Doschek, G. A. 2009, ApJ, 695, 36
Feldman, U., & Widing, K. G. 1990, ApJ, 363, 292
Fletcher, L., & Hudson, H. S. 2008, ApJ, 675, 1645
Fludra, A., & Schmelz, J. T. 1999, A&A, 348, 286
Freeland, S. L., & Handy, B. N. 1998, SoPh, 182, 497
Fu, H., Madjarska, M. S., Xia, L., et al. 2017, ApJ, 836, 169
Gloeckler, G., & Geiss, J. 1989, in AIP Conf. Proc. 183, Cosmic Abundances of Matter (Melville, NY: AIP), 49
Grevesse, N., Asplund, M., & Sauval, A. J. 2007, SSRv, 130, 105
Hayes, L. A., Gallagher, P. T., Dennis, B. R., et al. 2016, ApJL, 827, L30
Hoeksema, J. T., Liu, Y., Hayashi, K., et al. 2014, SoPh, 289, 3483
Jiang, C., Yan, X., Feng, X., et al. 2017, ApJ, 850, 8
Katsuda, S., Ohno, M., & Mori, K. 2020, ApJ, 891, 126
Kashyap, V., & Drake, J. J. 2000, BASI, 28, 475
Kawabata, Y., Inoue, S., & Shimizu, T. 2017, ApJ, 842, 106
Ko, Y.-K., Young, P. R., Muglach, K., Warren, H. P., & Ugarte-Urra, I. 2016, ApJ, 826, 126
Kohutova, P., & Verwichte, E. 2017, A&A, 602, A23
Kosugi, T., Matsuzaki, K., Sakao, T., et al. 2007, SoPh, 243, 3
Laming, J. M. 2004, ApJ, 614, 1063
Laming, J. M. 2009, ApJ, 695, 954
Laming, J. M. 2011, ApJ, 744, 115
Laming, J. M. 2015, LRSP, 12, 2

Laming, J. M., Vourlidas, A., Korendyke, C., et al. 2019, ApJ, 879, 124
Lemen, J. R., Title, A. M., Akin, D. J., et al. 2012, SoPh, 275, 17
Liu, R., Chen, J., Wang, Y., & Liu, K. 2016, NatSR, 6, 34021
Lodders, K., Palme, H., & Gail, H.-P. 2009, Abundances of the Elements in the Solar System , Vol. 4B (Berlin: Springer), 712
Luoni, M. L., Démoulin, P., Mandrini, C. H., & van Driel-Gesztelyi, L. 2011, SoPh, 270, 45
Mazzotta, P., Mazzitelli, G., Colafrancesco, S., & Vittorio, N. 1998, A&AS, 133, 403
McKenzie, D. L., & Feldman, U. 1992, ApJ, 389, 764
Milligan, R. O., Fleck, B., Ireland, J., Fletcher, L., & Dennis, B. R. 2017, ApJL, 848, L8
Morgan, H., & Druckmüller, M. 2014, SoPh, 289, 2945
Pesnell, W. D., Thompson, B. J., & Chamberlin, P. C. 2012, SoPh, 275, 3
Phillips, K. J. H., & Dennis, B. R. 2012, ApJ, 748, 52
Phillips, K. J. H., Sylwester, J., Sylwester, B., & Kuznetsov, V. D. 2010, ApJ, 711, 179
Stangalini, M., Baker, D., & Valori, G. 2021, RSPTA, 379, 20200216
Sterling, A. C., Doschek, G. A., & Feldman, U. 1993, ApJ, 404, 394
Sylwester, B., Phillips, K. J. H., Sylwester, J., & Kępa, A. 2015, ApJ, 805, 49
Torrence, C., & Compo, G. P. 1998, BAMS, 79, 61
Veck, N. J., & Parkinson, J. H. 1981, MNRAS, 197, 41
Warren, H. P. 1999, SoPh, 190, 363
Warren, H. P. 2014, ApJL, 786, L2
Xue, Z., Yan, X., Yang, L., Wang, J., & Zhao, L. 2017, ApJL, 840, L23
Yang, L., Yan, X., Li, T., Xue, Z., & Xiang, Y. 2017, ApJ, 838, 131